JOURNAL OF COMPUTATIONAL PHYSICS 22, 459–485 (1976)

Diffusively Induced Boundary Layers in a Tilted Square Cavity: A Numerical Study*

CHARLES QUON

Atlantic Oceanographic Laboratory, Bedford Institute of Oceanography, Dartmouth, Nova Scotia, Canada

Received February 11, 1976

The boundary layer flows induced in a stably stratified fluid by two opposite insulated boundaries of a tilted square cavity are studied by the finite difference method. The numerical solutions obtained agree reasonably well with the linear theory for high Rayleigh and high Prandtl number flow at two extreme angles of tilt. Two low Prandtl number flows, $\sigma = 10^{-1}$ and 10^{-3}, are included in the numerical solutions. The computational algorithm and its stability properties are discussed in some detail.

1. INTRODUCTORY REMARKS

Quon and Blumsack (in preparation) obtained boundary layer solutions for the two-dimensional free convection problem described below, and this study has been designed to test some of their results. Numerical solutions of seven finite difference computations are presented. Some of these solutions are not covered by the theory.

2. THE PROBLEM

In a stably stratified fluid (Fig. 1) where the tilted boundary is absent the whole is in static equilibrium. However, if an impermeable tilted boundary is present, the isopycnals bend through diffusive processes to meet the boundary at right angles. As a result, the fluid near the boundary is no longer in static equilibrium with the rest of the fluid because the static pressure there is less than it is at the same level in the interior of the fluid. Consequently, fluid creeps up the boundary in spite of the stable stratification. (Similarly, the fluid *under* a tilted boundary creeps *down*.) The resulting motion is called diffusively induced convection [6, 17].

* Bedford Institute of Oceanography Contribution.

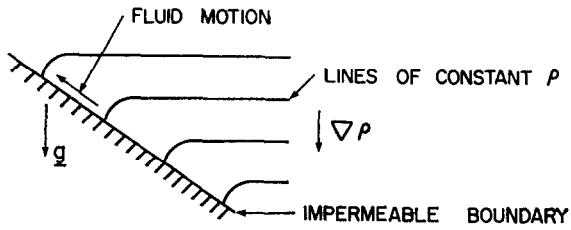

FIG. 1. Motion induced by an impermeable tilted boundary in a stably stratified fluid.

In both Phillips' and Wunsch's studies, the fluid medium is semi-infinite and the solutions can be assumed to be independent of the distance along the boundary. If the boundary is not infinitely long, but is terminated, say, by two more boundaries perpendicular to it, the solutions change drastically for some angles of tilt because of the other boundaries.

In the present study, a square cavity in the x–z plane as shown in Fig. 2 is considered. When it is rotated about the y-axi, the x-axis makes an angle ϕ with a fixed horizontal axis η. Consider the cavity to be filled with fluid. In order to induce convection diffusively, density variations are created by maintaining one side of the cavity at $z = 0$, at temperature $T_1 = S\xi(x, 0, \phi)$, and the opposite side at $z = 1$, at temperature $T_2 = S\xi(x, 1, \phi)$, where S is a positive constant, and $\xi(x, z, \phi)$ is the vertical distance from the η axis at the point (x, z) for a given angle ϕ. The other sides of the cavity on $x = 0$, 1 are insulated, i.e., $T_x = 0$. The range of ϕ under consideration is $0 < \phi \leqslant \pi/2$. It can be shown easily that convection must occur in the above configuration because of the tilted insulated boundaries.

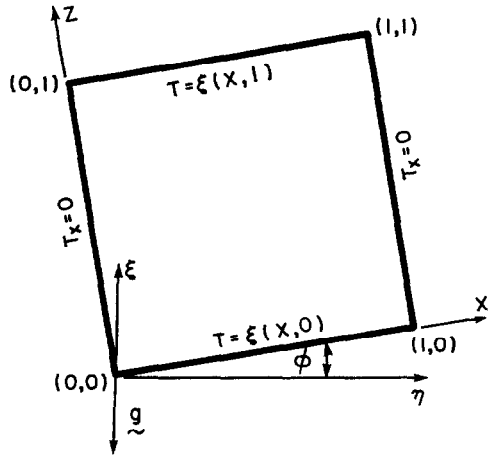

FIG. 2. The coordinate systems and the orientation of the cavity.

For large S, the induced flows are necessarily of boundary layer type. The two particular cases (for $\phi = 0$ and $\pi/2$) are almost exact analogies to the rotating cylinder problems studied by Stewartson [13]. $\phi = 0$ corresponds to Stewartsons' antisymmetric problem; $\phi = \pi/2$ corresponds to his symmetric problem. It has long been recognized [2, 16] that in certain circumstances stratification and rotation can produce equivalent effects. The present problem provides two specific examples.

3. The Solutions

To clearly present a comparison between numerical results and the boundary layer solutions, the analytical procedure and the boundary layer solutions are described briefly.

a. *The Equations*

The governing equations are the continuity equation, the Navier–Stokes equations, and the temperature equation. As two-dimensional motion is under consideration, a stream function, Ψ, can be used instead of the velocity components. Using Boussinesq approximation, it follows that

$$-(\partial/\partial t)\,\nabla^2\Psi + J(\nabla^2\Psi, \Psi) = -\nu\nabla^4\Psi - \alpha g(\partial T/\partial\eta), \tag{1}$$

$$(\partial/\partial t)T + J(\Psi, T) = \kappa\nabla^2 T, \tag{2}$$

where $\nabla^2 = \partial^2/\partial x_1^2 + \partial^2/\partial x_2^2$, $J(f, g) = (f_{x_1} g_{x_2} - g_{x_1} f_{x_2})$, and (x_1, x_2) stands for either (x, z) or (η, ξ).

The boundary conditions are

$$\begin{aligned} &T = S\xi, \\ &\Psi = \Psi_z = 0, && z = 0, L, \\ &T_x = \Psi = \Psi_x = 0, && x = 0, L, \end{aligned} \tag{3}$$

where L is the height and width of the cavity.

b. *Analytical Procedure*

Let (1) and (2) be nondimensionalized with (κ, L, SL) for (Ψ, X, T), where X represents the spatial coordinates. The nondimensional steady state equations are

$$(1/\sigma)\,J(\nabla^2\Psi, \Psi) = -\nabla^4\Psi - A(\partial T/\partial\eta), \tag{4}$$

$$J(\Psi, T) = \nabla^2 T. \tag{5}$$

$\sigma = \nu/\kappa$ is the Prandtl number, and $A = \alpha g S L^4/\kappa\nu$ is the Rayleigh number. The range of nondimensional temperature has become $0 \leqslant T \leqslant \xi(1, 1)$. (4) can be further simplified by considering $\sigma \to \infty$, and it is demonstrated later that $\sigma = 7$ can be thus approximated. The boundary conditions in (3) remain unaltered after nondimensionalization except those for T at $z = 0, 1$. The new conditions are $T = \xi$, where T and ξ are now nondimensional.

Because $T_0 = \xi$, and $\psi_0 =$ constant satisfy (4) and (5) and almost all the boundary conditions except those for T at $x = 0, 1$, we let $\Psi = \psi_0 + \psi$, and $T = T_0 + \theta$, where ψ and θ are corrections near the boundaries. In order to satisfy the boundary conditions, we require that: $\theta = 0$ at $z = 0, 1$, $\partial\theta/\partial x = -\partial T_0/\partial x$ and $x = 0, 1$; $\psi = -\psi_0$, and $\partial\psi/\partial N = 0$ on all boundaries, $\partial/\partial N$ being the normal derivative. Rewrite (4) and (5) in terms of ψ and θ and linearize (5) to give

$$\epsilon\nabla^4\psi = -(\cos\phi\theta_x - \sin\phi\theta_z), \tag{6}$$

$$\nabla^2\theta = -\sin\phi\psi_z + \cos\phi\psi_x, \tag{7}$$

where $\epsilon = A^{-1}$, which is taken to be a small number. In (6) and (7) $\xi = x\sin\phi + z\cos\phi$ and $\eta = x\cos\phi - z\sin\phi$ have been used. Equations (6) and (7) are solved for ψ and θ.

c. *Solutions for* $\phi \simeq 0$

For $\phi \simeq 0$, boundary layer solutions are obtained from either one of the following combined equations: $\epsilon\nabla^6\binom{\psi}{\theta} = -\cos^2\phi(\partial^2/\partial x^2)\binom{\psi}{\theta}$, provided that $\phi\epsilon^{-1/6} \ll 1$. The superscripts of the following solutions refer to the corresponding regions in Fig. 3 near either $x = 0$ or $z = 0$, or the corner adjacent to these two

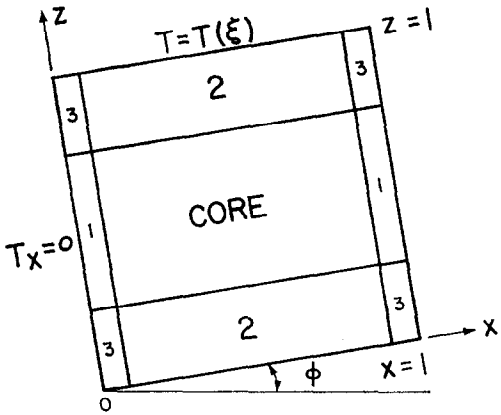

FIG. 3. The core and regions 1, 2, and 3 for boundary layer analysis.

boundaries (note that solution near other boundaries may require a change of sign).

$$\psi_0 = \tan\phi, \qquad T_0 = \xi, \tag{8a,b}$$

$$\psi^{(1)} = -\tan\phi e^{-\lambda\zeta}(\cos\lambda\zeta + \sin\lambda\zeta) + O(\epsilon^{1/4}), \tag{8c}$$

$$\theta^{(1)} = \epsilon^{1/4}\cdot(\sin\phi/\lambda)\, e^{-\lambda\zeta}\cos\lambda\zeta + O(\epsilon^{1/2}), \tag{8d}$$

$$\psi^{(2)} = \frac{-4}{\pi}\tan\phi \sum_{m=0}^{\infty} \frac{\sin(2m+1)\,\pi x}{(2m+1)}\,\chi_m(\gamma) + O(\epsilon^{1/3}), \tag{8e}$$

$$\theta^{(2)} = \epsilon^{1/3}\frac{8}{3^{1/2}}\sin\phi \sum_{m=0}^{\infty} \frac{\cos(2m+1)\,\pi x}{\sigma_m{}^2}\, e^{-1/2\sigma_m\gamma}\sin\frac{3^{1/2}}{2}\,\sigma_m\gamma + (\epsilon^{2/3}), \tag{8f}$$

$$\psi^{(*)} = \epsilon^{1/4}(4\tan\phi/\lambda)\, S(\gamma)\{1 - e^{-\lambda\zeta}\cos\lambda\zeta\}, \tag{8g}$$

$$\theta^{(*)} = \epsilon^{1/2}(4\sin\phi/\lambda^2)\, S(\gamma)\, e^{-\lambda\zeta}\{\cos\lambda\zeta + \sin\lambda\zeta\}, \tag{8h}$$

$$\psi^{(3)} = \psi_0 + \psi^{(1)} + \psi^{(2)} + \psi^{(*)}, \tag{8i}$$

$$T^{(3)} = T_0 + \theta^{(1)} + \theta^{(2)} + \theta^{(*)}, \tag{8j}$$

where

$$\lambda = (1/2\cos\phi)^{1/2},$$

$$\sigma_m = (2m+1)^{1/3}\,\pi^{1/3}\cos^{1/3}\phi,$$

$$\zeta = x\epsilon^{-1/4},$$

$$\gamma = z\epsilon^{-1/6},$$

$$\chi_m(\gamma) = e^{-1/2\sigma_m\gamma}[\cos(3^{1/2}/2)\,\sigma_m\gamma + (1/3^{1/2})\sin(3^{1/2}/2)\,\sigma_m\gamma],$$

$$S(\gamma) = \sum_{m=0}^{\infty}\chi_m(\gamma).$$

The solutions in the corner regions $\psi^{(3)}$ and $T^{(3)}$ in (8i) and (8j), satisfy the boundary conditions at $x = 0$, and asymptotically approach the solutions in the interior in regions 1 and 2. Since $\psi^{(*)} \sim O(\epsilon^{1/4})$, $\theta^{(*)} \sim O(\epsilon^{1/2})$, they are of the same order as the errors in $\psi^{(1)}$ and $\theta^{(1)}$. Hence

$$\psi^{(3)} = \psi_0 + \psi^{(1)} + \psi^{(2)} + O(\epsilon^{1/4}),$$

$$T^{(3)} = T_0 + \theta^{(1)} + \theta^{(2)} + O(\epsilon^{1/2}).$$

The negligibly small quantities $\psi^{(*)}$ and $\theta^{(*)}$ are shown in Fig. 14.

d. *Solutions for* $\phi = \pi/2$

The cases for $\phi \simeq \pi/2$, are governed by the combined equations: $\epsilon\nabla^6\binom{\psi}{\theta} = -\sin^2\phi(\partial^2/\partial z^2)\binom{\psi}{\theta}$. Nontrivial solutions are found near the insulated walls and

the corners, areas 1 and 3, are shown in Fig. 3. The solutions are valid provided that $(\pi/2 - \phi)\,\epsilon^{-1/6} \ll 1$:

$$\psi_0 = 0, \qquad T_0 = \xi, \tag{9a,b}$$

$$\psi^{(1)} = -(2/\mu)^{1/4}(z - \tfrac{1}{2})\exp\{-2^{1/4}\zeta_2\} + 1/\pi(2/\mu)^{1/4} \cdot \sum_{m-1}^{\infty}((-)^m \sin[\sigma_m{}^3(z - \tfrac{1}{2})]/m)\{e^{-\sigma_m\zeta_1} - 2e^{-\sigma_m\zeta_1/2}\cos(3^{1/2}/2)\,\sigma_m\zeta_1\} + O(\mu^{-1/6}), \tag{9c}$$

$$\theta^{(1)} = (\mu/2)^{1/4}\exp\{-2^{1/4}\zeta_2\} - \{2^{5/4}\mu^{5/12}\} \cdot \sum_{m=1}^{\infty}((-)^m \cos[\sigma_m{}^3(z - \tfrac{1}{2})]/\sigma_m{}^2) \cdot \{e^{-\sigma_m\zeta_1} - 2e^{-\sigma_m\zeta_1/2}\cos[(3^{1/2}/2)\,\sigma_m\zeta_1 + (2\pi/3)] + O(\mu^{1/2}) \tag{9d}$$

where $\mu = \epsilon^{1/2}$, $\sigma_m = (2m\pi)^{1/3}$, and ζ_1 and ζ_2 are of two different scales, $\zeta_1 = \mu^{-1/3}x$, $\zeta_2 = \mu^{-1/4}x$, which correspond to two different boundary layer thicknesses.

In area 3,

$$\psi^{(3)} = C(\zeta_2)\{1 - e^{-\gamma/2^{1/2}}(\cos\gamma/2^{1/2} + \sin\gamma/2^{1/2})\}, \tag{9e}$$

$$\theta^{(3)} = \mu^{1/2}2^{1/2} \cdot C(\zeta_2) \cdot \{1 - e^{-\gamma/2^{1/2}}\cos\gamma/2^{1/2}\}, \tag{9f}$$

where $\gamma = \mu^{-1/2}z$, or $\mu^{-1/2}(1 - z)$,

$$C(\zeta_2) = (8\mu)^{-1/4}\exp\{-2^{1/4}\zeta_2\}$$

Unlike the case for $\phi \simeq 0$, $\psi^{(2)}$ and $\theta^{(2)}$ are not required here on $z = 0, 1$ in area 2, because ψ_0 and T_0 in (9a, b) can satisfy the boundary conditions and the above solutions vanish as ζ_1 and $\zeta_2 \to \infty$.

e. *Solutions for Arbitrary ϕ*

Approximate solutions for arbitrary ϕ are being sought through the method of characteristics. Since these solutions are not yet finalized, only numerical solutions are discussed. Of particular interest is the case for $\phi = \pi/4$.

4. Method and Parameters of Computation

Instead of (4) and (5), the following time-dependent equations for the vorticity, ζ, and temperature T have been solved numerically

$$\nabla^2\psi = -\zeta, \tag{10}$$

$$(\partial/\partial t)\zeta + J(\psi, \zeta) = \sigma^{1/2}\nabla^2\zeta + A(\sin\phi(\partial/\partial z) - \cos\phi(\partial/\partial x))T, \tag{11}$$

$$(\partial/\partial t)T + J(\psi, T) = (1/\sigma^{1/2})\,\nabla^2 T, \tag{12}$$

subject to boundary conditions

$$\begin{aligned} T &= \xi, \quad \psi = \psi_z = 0 \quad \text{at} \quad z = 0, 1, \\ T_x &= 0, \quad \psi = \psi_x = 0 \quad \text{at} \quad x = 0, 1. \end{aligned} \tag{13}$$

In the above equations, $(\kappa\nu)^{1/2}$ instead of κ has been used as the characteristic stream function in order to use an existing computer program [9]. Therefore, the theoretical stream function will be divided by $\sigma^{1/2}$ before comparisons with the numerical solutions are made. The normalization constants for T and θ remain unchanged.

The finite difference method used for the computations and the stability analysis of the algorithm are discussed below. The integration procedure is to start with the condition $\zeta = \psi = 0$, $T = \xi$. Equations (10), (11), and (12) were integrated in cyclic order until steady state. A trial run with the initial conditions $\psi = \zeta = T = 0$ did not seem to affect the end result; however, it took much longer to reach steady state because of the slow diffusive processes.

Table I lists the parameters of computation. The choice of parameters is as follows: Cases 1, 3, and 5 are to give solutions at $\phi \simeq 0$, $\phi = \pi/4$, and $\phi = \pi/2$; cases 2 and 4 are to show how the solutions change from either extreme case towards $\pi/4$; cases 6 and 7 are for small Prandtl number flows to enhance the nonlinear effect of the system.

TABLE I
Parameters of Computation

Case	ϕ (deg)	A	σ $(=\nu/\kappa)$	$\kappa\nu$	Net
1	0.1	1.37×10^7	7.14	2.24×10^{-4}	40×40
2	5.0	1.37×10^7	7.14	2.24×10^{-4}	40×40
3	45.0	1.37×10^7	7.14	2.24×10^{-4}	40×40
4	80.0	1.37×10^7	7.14	2.24×10^{-4}	40×40
5	90.0	1.37×10^7	7.14	2.24×10^{-4}	40×40
6	90.0	1.37×10^7	1.0×10^{-1}	2.24×10^{-4}	40×40
7	90.0	1.37×10^7	1.0×10^{-2}	2.24×10^{-4}	40×40

a. *The Numerical Algorithm*

Equations (10), (11), and (12) subject to boundary condition (13) are approximated by finite differences on constant staggered grids as shown in Fig. 4.

The central idea of the finite difference scheme used here was first used by Lilly [4]. He and his colleagues in NCAR have used similar schemes for numerous computations of two-dimensional turbulence in subsequent years, (see [5]). The present author has also used it extensively to study convection problems in rotating

and nonrotating fluids [7, 8, 9, 11]. Although for convection problems of boundary layer type as described here, the present scheme has been superceded by a semi-implicit algorithm on variable grids [10]. The former scheme, which is used here, has retained its usefulness because of its simplicity. Furthermore, it is almost devoid of nonlinear instability.

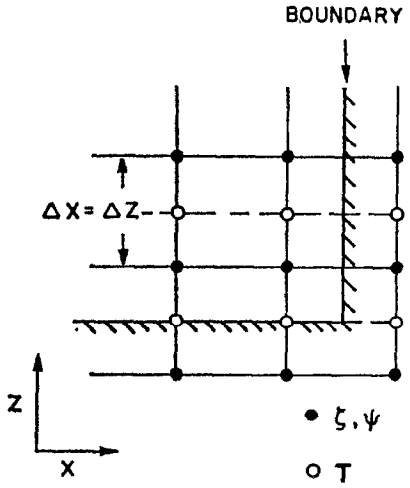

FIG. 4. Staggered constant grid used for the computation.

First consider Eqs. (11) and (12). They can be represented as

$$(\partial/\partial t)\mathbf{F} = \mathbf{H} \tag{14}$$

where

$$\mathbf{F} = \begin{pmatrix} \zeta \\ T \end{pmatrix}, \qquad \mathbf{H} = \begin{pmatrix} H_1 \\ H_2 \end{pmatrix} = \begin{pmatrix} J(\zeta, \psi) + \sigma^{1/2}\nabla^2\zeta + A(\sin\phi(\partial/\partial z) - \cos\phi(\partial/\partial x))T \\ J(T, \psi) + (1/\sigma^{1/2})\,\nabla^2 T \end{pmatrix}$$

For compact presentation, we shall use the familiar contracted notations:

$$\begin{aligned} G(x, z; t) &= G(j\,\Delta x, k\,\Delta z; \nu\,\Delta t) = G^{\nu}_{j,k}, \\ (\delta_t G)^{\nu+(1/2)}_{j,k} &= (1/\Delta t)(G^{\nu+1}_{j,k} - G^{\nu}_{j,k}), \\ (\delta_x G)^{\nu}_{j,k} &= (1/\Delta x)(G^{\nu}_{j+(1/2),k} - G^{\nu}_{j-(1/2),k}), \\ (\delta_z G)^{\nu}_{j,k} &= (1/\Delta z)(G^{\nu}_{j,k+(1/2)} - G^{\nu}_{j,k-(1/2)}), \\ \bar{G}^{\alpha} &= (G_{\alpha+(1/2)} + G_{\alpha-(1/2)})/2, \end{aligned} \tag{15}$$

α being ν, j, or k.

The finite difference representations for (14) are the following

$$(\delta_t \mathbf{F})^{\nu+1/2} = \tfrac{3}{2}\mathbf{H}^{\nu} - \tfrac{1}{2}\mathbf{H}^{\nu-1}. \tag{16}$$

(16) is centrally differenced in time at $t = (\nu + \frac{1}{2})\,\Delta t$, accurate to $O(\Delta t)^2$. It is a very simple algorithm to use because one can compute $\mathbf{H}^{\nu}$ and use it in (16) at one time level; then replace $\mathbf{H}^{\nu-1}$ in storage for use in the next time step. Equation (16) is the simplest form[1] of Adam–Bashforth representation for (14), which is well known for numerical solutions of ordinary differential equations [3].

Arakawa's quadratic conserving scheme [1] is used for the Jacobian in $\mathbf{H}$. Specifically the finite difference representation at time level ν is:

$$H^{\nu}_{1,j,k} = (1/3)\sum_{\alpha=1}^{3} J_\alpha(\zeta, \psi)^{\nu}_{j,k} + \sigma^{1/2}\nabla^2\zeta^{\nu}_{j,k} + A(\sin\phi\,\delta_z T^{\nu}_{j,k} - \cos\phi\,\delta_x \overline{T^{\nu}}^{xz}_{j,k}), \tag{17}$$

$$H^{\nu}_{2,j,k} = (1/3)\sum_{\alpha=1}^{3} J_\alpha(T, \psi)^{\nu}_{j,k} + (1/\sigma^{1/2})\,\nabla^2 T^{\nu}_{j,k}\,, \tag{18}$$

where

$$\begin{aligned} J_1(\zeta, \psi) &= \delta_x(\overline{\zeta}^{x}\delta_z\overline{\psi}^{xz}) - \delta_z(\overline{\zeta}^{z}\delta_x\overline{\psi}^{xz}),\\ J_2(\zeta, \psi) &= \delta_x\overline{\zeta}^{x}\delta_z\overline{\psi}^{z} - \delta_z\overline{\zeta}^{z}\delta_x\overline{\zeta}^{x},\\ J_3(\zeta, \psi) &= -\delta_x(\overline{\psi}^{x}\delta_z\overline{\zeta}^{xz}) + \delta_z(\overline{\psi}^{z}\delta_x\overline{\zeta}^{xz}), \end{aligned} \tag{19}$$

and

$$\begin{aligned} J_1(T, \psi) &= \delta_x(\overline{T}^{x}\delta_z\overline{\psi}^{x}) - \delta_z(\overline{T}^{z}\delta_x\overline{\psi}^{x}),\\ J_2(T, \psi) &= \delta_x\overline{T}^{x}\delta_z\psi - \delta_z\overline{T}^{z}\delta_x\overline{\psi}^{xz},\\ J_3(T, \psi) &= -\delta_x(\overline{\psi}^{xz}\delta_z\overline{T}^{xz}) + \delta_z(\psi\delta_x\overline{T}^{z}). \end{aligned} \tag{20}$$

The subscripts j, k, and the superscript ν have been suppressed. Note that although the Jacobian representations J_1, J_2, and J_3 in (19) and (20) are identical in differential form, they utilize different combinations of grid points in finite difference form. The spatial differences are central differences about ζ in (19) and about T in (20).

Square nets of $M \times M$ points are used, i.e., $1 \leqslant j \leqslant M$, $1 \leqslant k \leqslant M$. While the ψ and ζ fields span over the whole range of $M \times M$ points, the T-field occupies only $M \times (M - 1)$ points, i.e., $1 \leqslant j \leqslant M$, $1 \leqslant k \leqslant (M - 1)$. The boundary conditions are approximated as follows

$$\begin{aligned} T_{j,1} &= \xi(x, 0; \phi) = (j-1)\,\Delta x \sin\phi, \qquad \text{at} \quad z = 0,\\ T_{j,N-1} &= \xi(x, 1; \phi) = (j-1)\,\Delta x \sin\phi + \cos\phi, \qquad \text{at} \quad z = 1,\\ T_{1,k} &= T_{2,k}\,, \qquad T_{M,k} = T_{M-1,k}\,, \qquad \text{for all } k, \end{aligned}$$

[1] The next level of approximation by Adam–Bashforth expansion is $(\delta_t \mathbf{F})^{\nu+(1/2)} = (1/12)(23\mathbf{H}^{\nu} - 16\mathbf{H}^{\nu-1} + 5\mathbf{H}^{\nu-2})$.

$\psi = 0$ on the outermost 2 layers of points in the net. ζ on the outermost layers are not used. ζ on the second outermost layers of points, ζ_2 are obtained from

$$\zeta_2 = -(\delta_x{}^2\psi + \delta_z{}^2\psi)_2 = -(\psi_3/h^2),$$

where ψ_3 is the nearest nonzero neighbour of ζ_2, and h is either Δx or Δz. The four corner points, ζ_2, are the average of their two nearest neighbors defined above. This rather crude approximation of the boundary conditions for ψ and ζ has yielded some reasonably accurate results.

When the mesh points are sufficiently dense, the error in ψ can be kept small. Obviously the error in ψ depends on the configuration of the flow field, because this approximation not only shifts the boundary points one half grid points inward, amounting to adding or subtracting some values from ψ at these points, it also assumes $\partial\psi/\partial\lambda = 0$ at half a grid distance inside the physical boundaries, $\partial/\partial\lambda$ being in the direction along the boundaries.

In the context of our problem this latter assumption is in line with the solutions of case 1, but may produce considerable error for case 5 because ψ for that case varies along the boundaries. It is expected that the errors are contained when h is small.

b. *Stability Property*

The full set of Eqs. (16) to (20) are too complicated to analyze for stability criteria. Instead, a set of linear equations appropriate to the problem is analyzed. Consider

$$-\delta_t\nabla^2\psi = -(\sigma)^{1/2}\,\nabla^4\psi + A\sin\phi\delta_z T - A\cos\phi\delta_x\overline{T}^{xz}, \tag{21}$$

$$\delta_t T = (1/\sigma^{1/2})\,\nabla^2 T - \sin\phi\delta_z\psi + \cos\phi\delta_x\overline{\psi}^{xz}, \tag{22}$$

where $\nabla^2 = (\delta_x{}^2 + \delta_z{}^2)$, $\nabla^4 = (\delta_x{}^2 + \delta_z{}^2)^2$. Expanding ψ and T at grid point (j, k) by Fourier series yields

$$\begin{pmatrix}\psi_{j,k}\\ T_{j,k}\end{pmatrix} = \sum_{l,m}\begin{pmatrix}\psi_{lm}\\ T_{lm}\end{pmatrix}\exp\{i(jl + km)\,h\pi\}, \qquad \text{with} \quad h = \Delta x = \Delta z, \quad i = (-1)^{1/2}.$$

The following identities are used for the spatial operators in (21) and (22):

$$\begin{aligned}(\delta_x{}^2 + \delta_z{}^2) &\equiv -(4/h^2)(\sin^2 lh\pi/2 + \sin^2 mh\pi/2),\\ \delta_x(-)^{xz} &\equiv i(1/h)\cos mh\pi/2\sin lh\pi,\\ \delta_z &\equiv i(2/h)\sin mh\pi/2.\end{aligned} \tag{23}$$

Thus, for arbitrary l, m within the range $1 \leqslant l, m \leqslant 1/h$,

$$\begin{aligned}\delta_t\psi_{lm} &= -(\sigma)^{1/2}\,\alpha^2\psi_{lm} + i(A\beta/\alpha)\,T_{lm},\\ \delta_t T_{lm} &= -(\alpha/\sigma^{1/2})\,T_{lm} - i\beta\psi_{lm},\end{aligned} \tag{24}$$

where

$$\alpha = (4/h^2)(\sin^2 lh\pi/2 + \sin^2 mh\pi/2),$$
$$\beta = (1/h)(2 \sin \phi \sin mh\pi/2 - \cos \phi \cos mh\pi/2 \sin lh\pi). \tag{25}$$

Applying the Adam–Bashforth scheme on (24) yields

$$\begin{aligned}(1/\Delta t)(\psi_{lm}^{\nu+1} - \psi_{lm}^{\nu}) &= \alpha\sigma^{1/2}((3/2)\,\psi_{lm}^{\nu} - (1/2)\,\psi_{lm}^{\nu-1}) + i(A\beta/2)((3/2)\,T_{lm}^{\nu} - (1/2)\,T_{lm}^{\nu-1}),\\ (1/\Delta t)(T_{lm}^{\nu+1} - T_{lm}^{\nu}) &= -i\beta((3/2)\,\psi_{lm}^{\nu} - (1/2)\,\psi_{lm}^{\nu-1}) - (\alpha/\sigma^{1/2})((3/2)\,T_{lm}^{\nu} - (1/2)\,T_{lm}^{\nu-1}),\end{aligned} \tag{26}$$

which can be written as the following with lm on ψ and T dropped

$$\mathbf{F}^{\nu+1} = S_{lm}\mathbf{F}^{\nu},$$
$$(\mathbf{F}^{\nu+1})^{\hat{T}} = (\psi^{\nu+1}, \psi^{\nu}, T^{\nu+1}, T^{\nu}),$$

where $\hat{T}$ indicates the transpose. S_{lm} is the amplification matrix

$$S_{lm} = \begin{pmatrix} 1 - \Delta t\dfrac{3\alpha\sigma^{1/2}}{2} & \Delta t\dfrac{\alpha\sigma^{1/2}}{2} & i\Delta t\dfrac{3A\beta}{2\alpha} & -i\Delta t\dfrac{A\beta}{2\alpha} \\ 1 & 0 & 0 & 0 \\ -i\Delta t\dfrac{3\beta}{2} & i\Delta t\dfrac{\beta}{2} & 1 - \Delta t\dfrac{3\alpha}{2\sigma^{1/2}} & \Delta t\dfrac{\alpha}{2\sigma^{1/2}} \\ 0 & 0 & 1 & 0 \end{pmatrix}. \tag{27}$$

For stability we require

$$\lambda_{lm}^{*}\lambda_{lm} \leqslant 1,$$

where λ_{lm} is an eigenvalue of S_{lm}, and λ_{lm}^{*} is its complex conjugate.

For practical purposes, it is not necessary to study the general property of matrix (27). To simplify the analysis, the diffusion limit of (27) is examined by setting $\beta = 0$. The eigenvalues of (27) for $\beta = 0$ are the roots of the following characteristic equation:

$$\{(1 - \tfrac{3}{2}a_1 - \lambda)(-\lambda) - \tfrac{1}{2}a_1\}\{(1 - \tfrac{3}{2}a_2 - \lambda)(-\lambda) - \tfrac{1}{2}a_2\} = 0,$$

where $a_1 = \Delta t\alpha\sigma^{1/2}$, $a_2 = \Delta t\alpha/\sigma^{1/2}$. The four roots are

$$\lambda_{i\pm} = \tfrac{1}{2}(1 - \tfrac{3}{2}a_i) \pm \tfrac{1}{2}\{(1 - \tfrac{3}{2}a_i)^2 + 2a_i\}^{1/2}, \qquad i = 1, \text{ or } 2.$$

Clearly all λ_i are real for $a_i \geqslant 0$, and

$$|\lambda_i| \leqslant 1 \qquad \text{if} \qquad a_i \leqslant 1.$$

From (25a), $\max \alpha = 8/h^2$, hence $a_i \leqslant 1$ imposes a limit on Δt as

$$\begin{aligned} \Delta t/h^2 &\leqslant (1/8\sigma^{1/2}) \quad \text{for} \quad \sigma \geqslant 1, \\ \Delta t/h^2 &\leqslant \sigma^{1/2}/8 \quad \text{for} \quad \sigma \leqslant 1. \end{aligned} \tag{28a, b}$$

These conditions for Δt are not much more stringent than other explicit schemes accurate to $O(\Delta t^2)$ (see [12, p. 189]). For $h = 1/38$ as used in our computations, (28a, b) give the following numerical upper limits for Δt

$$\begin{aligned} \Delta t &\leqslant 3.24 \times 10^{-5} \quad \text{for} \quad \sigma = 7.14, \\ \Delta t &\leqslant 2.73 \times 10^{-6} \quad \text{for} \quad \sigma = 10^{-3}. \end{aligned}$$

Figure 5 plots (1) the complete set of four eigenvalues of (27) for $\sigma = 7.14$, $lh = mh = 1$ and $\phi = \pi/2$ to give maximum values for α and β. All eigenvalues are real and three of them have absolute values less than unity for $\Delta t \leqslant 10^{-4}$ as shown. The fourth, λ_4, is equal to -1 at $\Delta t \simeq 3.24 \times 10^{-5}$, the same as the diffusion limit calculated above. This is not unexpected because if S_{lm} is partitioned such that $S_{lm} = \begin{pmatrix} s_1 & s_2 \\ s_3 & s_4 \end{pmatrix}$, where the block elements are 2×2 matrices, s_3 has much smaller elements than the other for large A and M. Hence the effectual eigenvalues

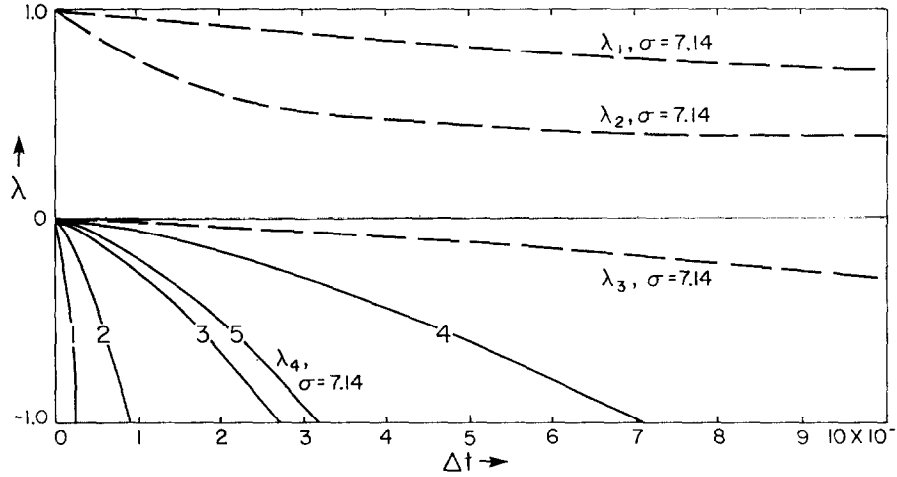

FIG. 5. Eigenvalues of matrix (27) for $\Delta t \leqslant 10^{-4}$ for different values of σ. For $\sigma = 7.14$, all four eigenvalues are plotted as functions of Δt. Curves 1 to 4 represent the eigenvalues of $\sigma = 10^{-3}, 10^{-2}, 10^{-1}$, and 1. All the three other eigenvalues are less than unity and are not shown. Note that curve 1 also represents the eigenvalue for $\sigma = 10^3$ (with the largest modulus). This is expected if σ deviates much from unity, because the dominant diagonal term contains $\sigma^{1/2}$ for σ large, and $1/\sigma^{1/2}$ for σ small.

of S_{lm} are those of s_1 and s_4. (2) λ_4 for $\sigma = 1.0, 10^{-1}, 10^{-2}, 10^{-3}$, and 10^3. The rest of the eigenvalues have absolute value less than unity for $\Delta t \leqslant 10^{-4}$ investigated. All eigenvalues are real. It is worth noting that except for $\sigma = 1.0$, the maximum Δt for all other values of σ are very close to the diffusion limit given by (28). Even for $\sigma = 1$, the diffusion limit of 8.66×10^{-5} has been lowered by only 18% to 7.07×10^{-5}. The maximum Δt is at $\sigma = 1.0$ as indicated by (28).

It is also interesting to note that even for case 7, whose velocity fields are very strong, the limit for Δt is still the diffusion limit. The nondimensional maximum U for case 7 is $\simeq 10^3$. The advection limit would be $\Delta t \leqslant (h/4U) = 6.58 \times 10^{-6}$, which is still less stringent than the diffusion limit. It is clear that for the type of problem studied here some kind of semi-implicit treatment of the diffusive term can be used to great advantage as already demonstrated in [10].

Figure 6 depicts the results of two numerical experiments using the full equations to determine the maximum Δt that can be used for a given set of parameters. The ordinate represents the number of cycles a computation can attain for a Δt before

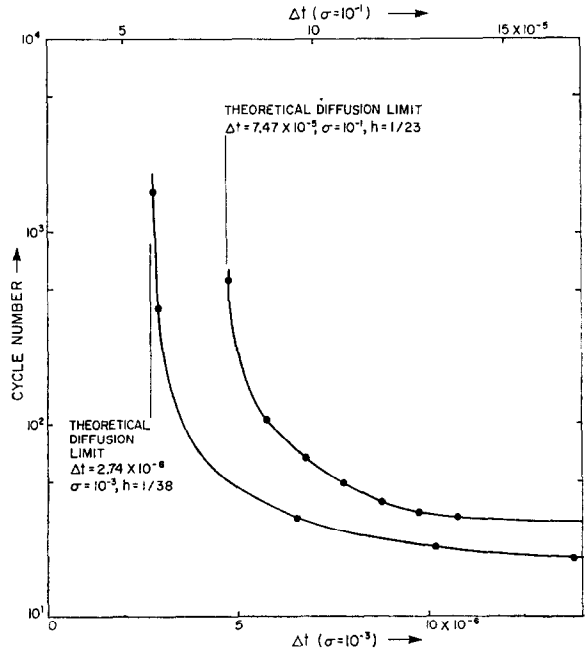

FIG. 6. Results of direct numerical experiments with Eqs. (26) and (30). The two solid curves show the cycle numbers at which the computations "blew up." Note these cycle numbers are only rough indications for any given Δt. They both approach asymptotic values close to the diffusion limits indicated by the vertical lines.

the computation "blows up." These crude experiments give amazingly good estimates. Note that for both cases, the theoretical diffusion limits almost coincide with the vertical asymptotes of the experimental curves.

c. *Solving the Poisson's Equation*

In addition to (11) and (12), (10) must be solved at each time step. Very efficient direct and iterative methods are available for its solution. Here we have used the ADI method [15, p. 209, and references]. Instead of a set of acceleration parameters usually derived from a min-max problem for ADI, we used the exact eigenvalues of the iterative matrices. Perhaps eigenvalues are not the most efficient acceleration parameters, but they are very simple to use. We shall describe what they are and what the results are by using them as acceleration parameters. Equation (10) can be written in a 5-point finite difference form as follows:

$$(\psi^{\nu}_{j+1,k} + \psi^{\nu}_{j-1,k} + \psi^{\nu}_{j,k+1} + \psi^{\nu}_{j,k-1} - 4\psi^{\nu}_{j,k}) + h^2\zeta^{\nu}_{j,k} = 0 + R_{j,k}\,, \tag{29}$$

where the maximum of $R_{j,k}$, the residue, can be prescribed. The procedure is to separate one complete iteration into two consecutive steps as follows:

$$\begin{aligned}\psi^{n+(1/2)}_{j+1,k} - 2\psi^{n+(1/2)}_{j,k} + \psi^{n+(1/2)}_{j-1,k} - \lambda_n\psi^{n+(1/2)}_{j,k} \\ = -(\psi^{n}_{j,k+1} - 2\psi^{n}_{j,k} + \psi^{n}_{j,k-1} + \lambda_n\psi^{n}_{j,k}) - h^2\zeta^{\nu}_{j,k}\,,\end{aligned} \tag{30a}$$

$$\begin{aligned}\psi^{n+1}_{j,k+1} - 2\psi^{n+1}_{j,k} + \psi^{n+1}_{j,k-1} - \lambda_n\psi^{n+1}_{j,k} \\ = -(\psi^{n+(1/2)}_{j+1,k} - 2\psi^{n+(1/2)}_{j,k} + \psi^{n+(1/2)}_{j-1,k} + \lambda_n\psi^{n}_{j,k}) - h^2\zeta^{\nu}_{j,k}\,.\end{aligned} \tag{30b}$$

Equation (30a) can be solved for all k and then (30b) can be solved for all j by Gaussian elimination. For each ν, we need to iterate (30) n times for n as large as necessary for (29) to be satisfied. λ_n are the acceleration parameters for the nth iteration. If we represent the error after each semi-iteration by $E^{n+(1/2)}_{lm}\exp\{i(jl + km)\,h\pi\}$ and $E^{n+1}_{lm}\exp\{i(jl + km)\,h\pi\}$, they satisfy (30) without the terms containing ζ^{ν}. The error equations can be written as

$$\begin{pmatrix} E^{n+1}_{lm} \\ E^{n+(1/2)}_{lm} \end{pmatrix} = -(A + \lambda_n I)^{-1}\,(B - \lambda_n I)\begin{pmatrix} E^{n+(1/2)} \\ E^{n} \end{pmatrix}, \tag{31}$$

where

$$A = \begin{pmatrix} a_m & 0 \\ 0 & b_l \end{pmatrix}, \qquad B = \begin{pmatrix} b_l & 0 \\ 0 & a_m \end{pmatrix}, \qquad I = \begin{pmatrix} 1 & 0 \\ 0 & 1 \end{pmatrix}, \qquad \begin{pmatrix} a_m \\ b_l \end{pmatrix} = \begin{pmatrix} 4\sin^2 mh\pi/2 \\ 4\sin^2 lh\pi/2 \end{pmatrix}.$$

l, m are independent wave numbers and $1 \leqslant l, m \leqslant M$. M being the total number of grid *intervals* in a unit square, or $Mh = 1$. $(A + \lambda_n I)^{-1}$ exists if $(-\lambda_n)$ is not an eigenvalue of A. Theoretically if we choose λ_n equal to either one of the two eigenvalues of B, i.e., $\lambda_n = a_n$, or b_n, $1 \leqslant n \leqslant M$, we remove all error after M complete iterations. For large M, this procedure is clearly inefficient. In practice,

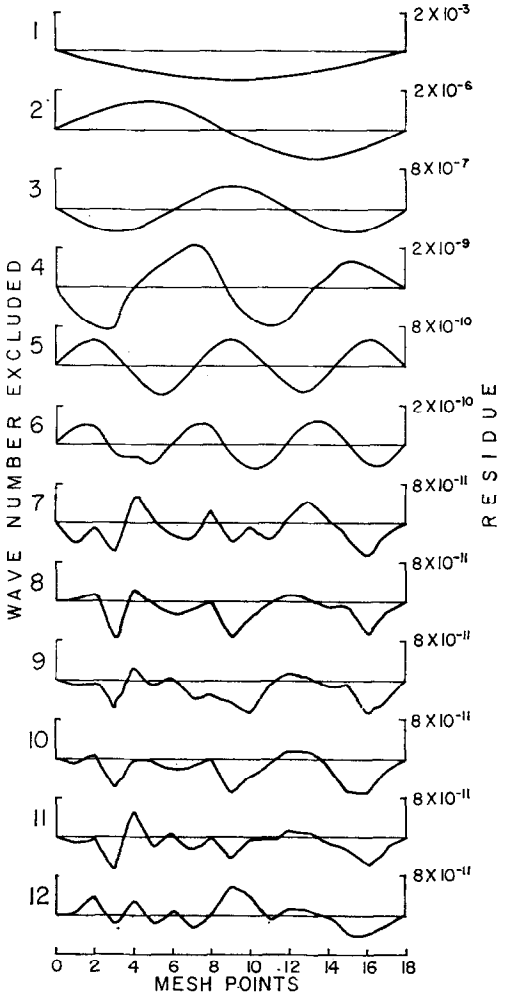

FIG. 7. Numerical experiments with the Poisson's equation (30). Numbers on the left-hand side indicate the missing wave number used in computing the acceleration parameters. Note

however, we need only to iterate with the 3 or 4 lowest wave numbers each, even for M as large as 40.

In order to see whether or not λ_n would remove the nth component of the error, a series of numerical experiments are performed as follows. A random field ζ with magnitude $O(1)$ is introduced into a unit square, and (30) is solved for ψ with $(M-1)$ iterations. Progressively one wave number was left out in the set of parameters used: the first run uses $a_2, a_3, a_4, \ldots, a_M$ in $(M-1)$ iterations; the second run used $a_1, a_3, a_4, \ldots, a_M$, etc. In Figure 7, the residues along the center line at $z = \frac{1}{2}$ for $M = 18$ are plotted. From top to bottom, the runs are for consecutive missing wave numbers. It is clear that the residues correspond to the wave number excluded in the acceleration parameters. Note that $\zeta \sim O(1)$, $h^2 \sim (10^{-3})$, $R \sim O(10^{-11})$ would give $\Delta\psi/\psi \sim O(10^{-8})$, which is about the machine accuracy.

In computing ψ in consecutive time steps, one additional advantage is to use ψ in the previous time step as the initial condition. Experience has indicated that using the first 3 or 4 wave numbers gives reasonably accurate results.

5. Numerical Results

For high Rayleigh number flows ($A \to \infty$), the nondimensional boundary layer thicknesses range from $\epsilon^{1/4}$ to $\epsilon^{1/8}$. To produce boundary layer flow, $\epsilon^{1/8}$ must be sufficiently small for separation and $\epsilon^{1/4}$ must be sufficiently large for grid resolution. For $A = 1.37 \times 10^7$, we have $\epsilon^{1/8} = 1.28 \times 10^{-1}$ and $\epsilon^{1/4} = 1.64 \times 10^{-2}$. In a unit square, the boundary layers are separated widely enough, but 40×40 nets of constant grid interval ($\Delta = 1/38 = 2.63 \times 10^{-2}$), though apparently insufficiently dense to give good resolution, gave results that agree reasonably well with the theory.

a. *High Rayleigh Number, High Prandtl Number Flows*

Figure 8 depicts the four basic fields, T, θ, ψ and ζ, of cases 1 to 5. The true vertical is opposite to the gravitational vector shown at the lower left corner of Row d. In all cases the interior isotherms in Row a indicate the true horizontal.

Row a is the total temperature field. Row b is obtained from the total temperature field by subtracting $T_0 = \xi$ from it. Hence Row b represents the boundary layer field θ.

i. *The Cases with $\phi \simeq 0$.* The θ and ψ contours of case 1 in Fig. 8 give a good illustration of its boundary layer formation. The thermal boundary layer is stronger near the insulated walls at $x = 0, 1$ than that near the heated walls at $z = 0, 1$. The theory (8d and 8f) predicts their relative magnitudes to be $O(\epsilon^{1/4})$

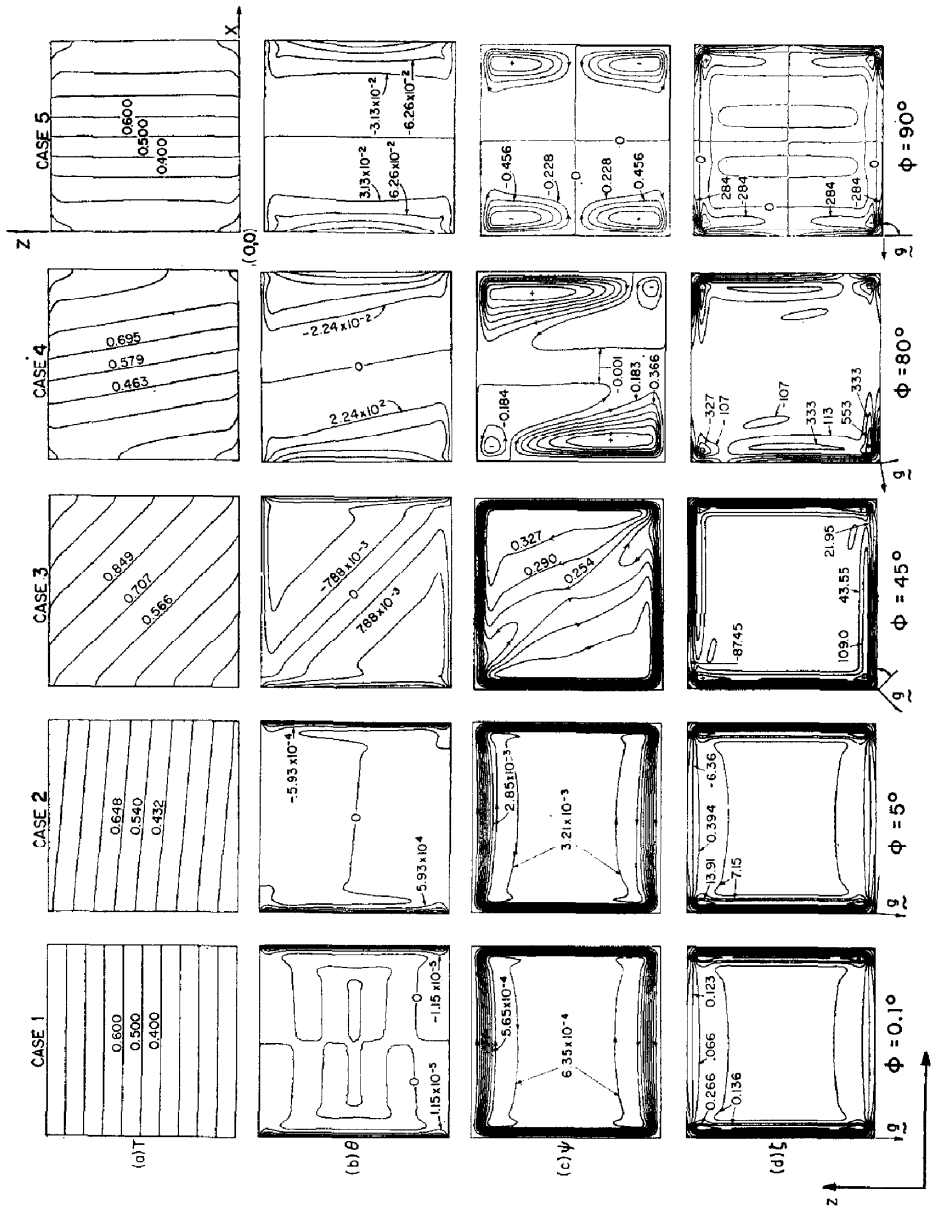

FIG. 8. Contours of cases 1 to 5: (a) T, the total temperature, (b) the induced temperature $\theta(=T-\xi)$, (c) ψ, the stream function, (d) ζ, the vorticity. Contour intervals are constant. They can be obtained as the difference between any adjacent intervals.

and $O(\epsilon^{1/3})$, and their width to be $O(\epsilon^{1/4})$ and $O(\epsilon^{1/6})$. According to (8d) and (8f), the $\epsilon^{1/4}$ layer, ($\theta^{(1)}$ at $x = 0, 1$), is independent of z, while the $\epsilon^{1/6}$ layer ($\theta^{(2)}$ at $z = 0, 1$), is antisymmetric about $x = \frac{1}{2}$. Although $\theta^{(1)}$ is stronger than $\theta^{(2)}$, $\theta^{(2)}$ is a broader layer, and hence is more likely to extend further into the interior than $\theta^{(1)}$.

According to (8c) and (8e), $\psi^{(1)}$, the $\epsilon^{1/4}$ layer near $x = 0, 1$, is independent of z, while $\psi^{(2)}$, the $\epsilon^{1/6}$ layer, should bulge toward the interior near $x = \frac{1}{2}$. Again because $\psi^{(2)}$ is a broader layer than $\psi^{(1)}$, it is more likely that $\psi^{(2)}$ not $\psi^{(1)}$ influences the interior. Figure 9a shows the details of $\theta^{(2)}$ and its extension into the interior while Fig. 9c shows the stream function in the interior, which can be interpreted as the extension from $\psi^{(2)}$.

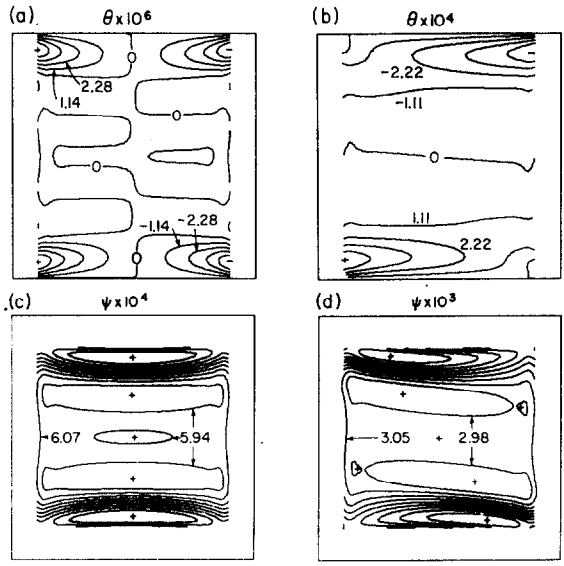

FIG. 9. Detailed contours of the interior θ and ψ for cases 1 and 2. The stronger boundary layer values have been blocked off so that the details of the weak interior distribution can be contoured.

Case 2 in Fig. 8 shows the changes in the various fields when the angle of tilt is increased from 0.1° to 5°. The overall features are very similar to those for case 1. The changes are visible, however; Figs. 9b and d show the interior θ and ψ of case 2. θ is no longer antisymmetric, and ψ is no longer symmetric about $x = \frac{1}{2}$. For the theory to be valid, $\phi\epsilon^{-1/6} \ll 1$ must hold. For case 1, $\phi\epsilon^{-1/6} = 0.027$, while for case 2, $\phi\epsilon^{-1/6} = 1.35$.

ii. *Cases with* $\phi \simeq \pi/2$. For $\phi = \pi/2$, the theory produces double boundary layers near the insulated walls at $x = 0, 1$. The inner layer has a thickness of $O(\mu^{1/3})$, and the outer layer of $O(\mu^{1/4})$, and these layers correspond respectively to the two parts containing $\zeta_1 (= z\mu^{-1/3})$ and $\zeta_2 (= z\mu^{-1/4})$ in (9c) and (9d).

The outer thermal layer is independent of z while the inner layer has a maximum (or minimum) at $z = \frac{1}{2}$ as shown in Eq. (9d). Both the inner and outer layer of the stream function $\psi^{(1)}$ in (9c) are antisymmetric about $z = \frac{1}{2}$. The four-cell formation as shown in Fig. 8c of case 5 is contained in (9c) and (9e). Equations (9e) and (f) both represent a thinner end layer that satisfy the boundary conditions at $z = 0, 1$ and match the main boundary layers.

Case 4 is for $\phi = 80°$. The most obvious difference between cases 4 and 5 is that θ and ψ of case 4 are no longer symmetric or antisymmetric about $z = \frac{1}{2}$. The ψ-cells at the pivoting corner and the cell diagonally across become more dominant. As the angle of tilt is reduced from 90°, the induced convection must go up along the insulated boundary at $x = 0$ and down at $x = 1$ as established in Section 2. This explains why two cells can dominate the others as shown for case 4 because they have the preferred circulation. It is difficult, however, to extrapolate these solutions to explain the flow in case 3 which we shall consider next.

iii. *Case with* $\phi \simeq \pi/4$. Case 3 is for $\phi \equiv \pi/4$. The flow in this case is difficult to analyze. There are four boundary layers seemingly of equal strength and equal width along all four boundaries. Unlike either case 1 or case 5 whose interiors can be considered motionless, the leakage from the boundary layers contribute higher order flows in the interior that are not entirely along the isotherms. The θ diagram shows that θ is also nonzero in the interior, but like T_0, θ is not a function of η and hence cannot generate any motion. Thus, we must conclude that the interior is diffusive as well as conductive. This case has not yet been successfully analyzed.

b. *High Rayleigh Number, Low Prandtl Number Flow*

The effect of the advective term in (4) can become negligible as $\sigma \to \infty$. It has been shown in earlier studies of convection in a cavity [9] that even for $\sigma \sim O(1)$, the momentum equation can be linearized. Two cases with $\sigma = 10^{-1}$, case 6, and $\sigma = 10^{-3}$, case 7, are presented and the effect of small σ is examined.

Figure 10 depicts the four basic fields of cases 6 and 7. Both cases are for $\phi = \pi/2$. The contoured fields of cases 5 and 6 appear similar, but the magnitude of θ has increased by 50% and the maxima of ψ has increased by 90% for case 6. Though σ changes, all other characteristic values remain constant for cases 5, 6, and 7. Therefore, it is meaningful to compare the nondimensional field values (see Table I).

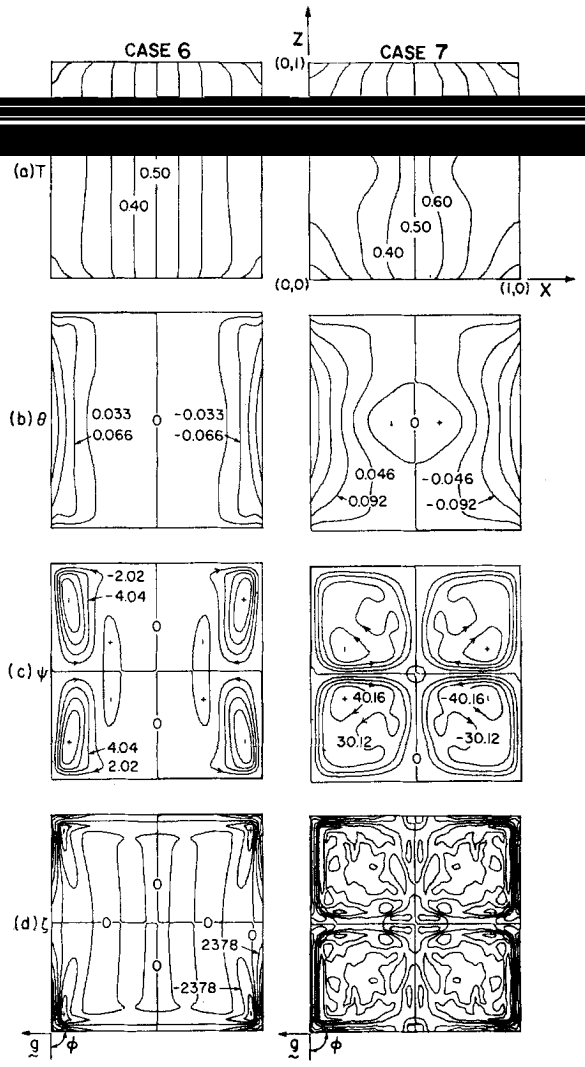

FIG. 10. Contours of cases 6 and 7 (see caption of Fig. 4 for explanation).

Case 7, with $\sigma = 10^{-3}$, is very different. Figure 10 shows that instead of boundary layer cells, the motion occupies the whole cavity. The maximum θ has increased to 0.23 in comparison with the overall imposed temperature of unity. Nonlinearity has dominated the flow. Figure 11 shows the temporal development of various terms in (11) at a point near the bottom insulated boundary. Note that case 7

cannot attain steady state. The final dynamical balance is between $\partial\zeta/\partial t$ and $J(\psi, \zeta)$. The vorticity field shown in Fig. 10 is chaotic and looks more like that of a turbulent than laminar flow.

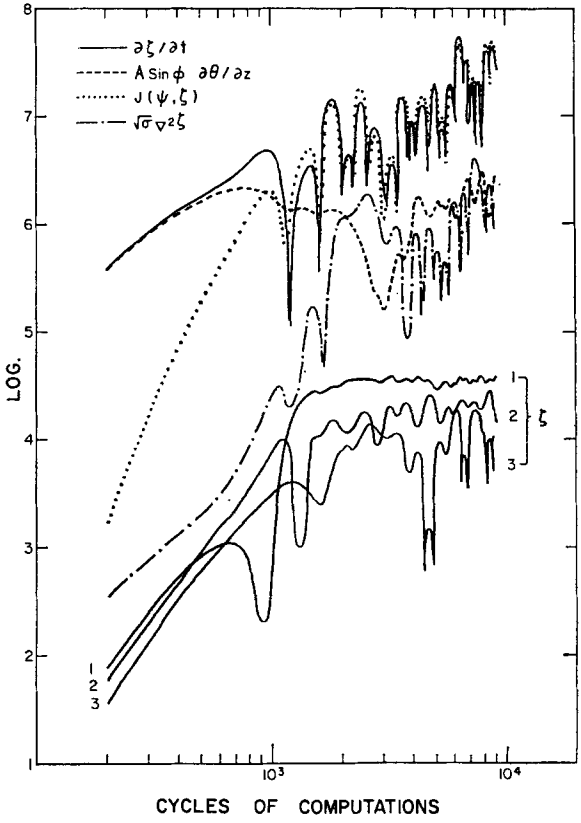

FIG. 11. Temporal development of Eq. (11) for case 7, $\sigma = 10^{-8}$ at the point $x = 0.145$, $z = 0.224$ (upper four curves). The lower three curves are for the vorticity at three adjacent points, $z = 0.224$, $x = 0.039$, 0.090, and 0.145, which are consecutively numbered 1, 2, and 3.

Figure 12 shows the three-dimensional plots of Fig. 10. Of particular interest are the θ fields. For case 7, the center of θ starts to deform. While this kind of plot does not add any dynamical understanding, it provides a new dimension that may reveal small but interesting features of the fields one could otherwise overlook.

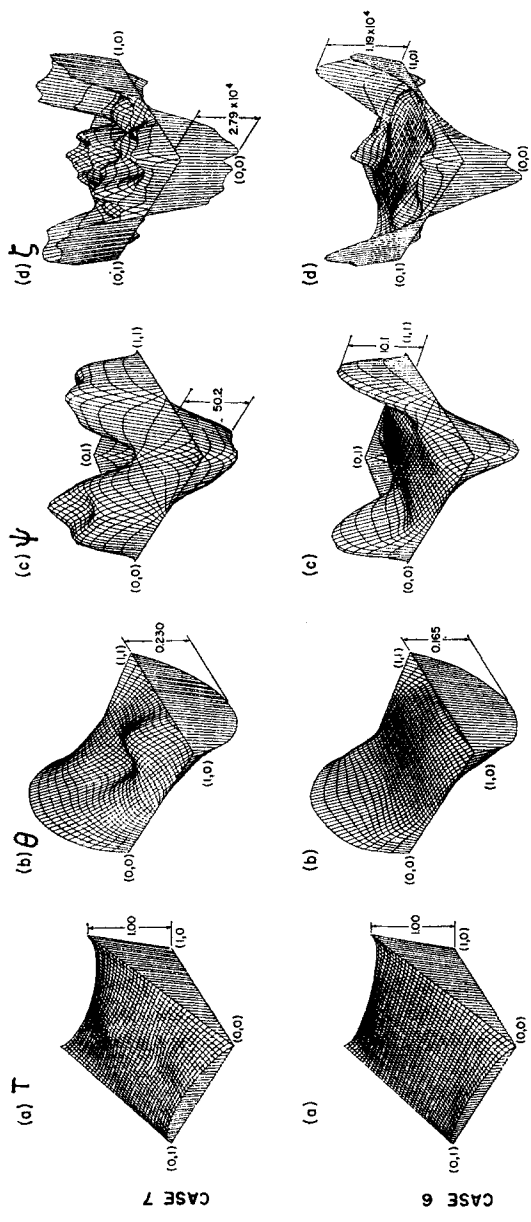

FIG. 12. Three-dimensional plots of T, θ, ψ, and ζ for cases 6 and 7. The viewing direction for diagrams (a) and (d) is diagonally from the corner at $(x, z) = (0, 0)$, and that for (b) and (c) is from $(x, z) = (1, 0)$ (see coordinates in the upper right diagram of Fig. 10).

6. Comparison between Theory and Computation

i. *Case* 1, $\phi = 0.10°$

The specific solutions to be compared with the computations are (8). These solutions are relatively easy to compare graphically.

Figure 13 shows the structure of the two fields across the two layers on the boundaries near $x = 0$, (Figs. 13a and b) and near $z = 0$ (Figs. 13c and d). The functional forms of the analytical and finite difference solutions are very similar. There is, however, a difference of about 8 % between the theory and the computation in both the temperature and the stream function. There are two sources for the discrepancy: (1) errors from the finite difference approximation, and (2) errors allowed in the analytical solutions, which are $O(\epsilon^{1/4})$. The precise magnitude cannot be obtained for either error.

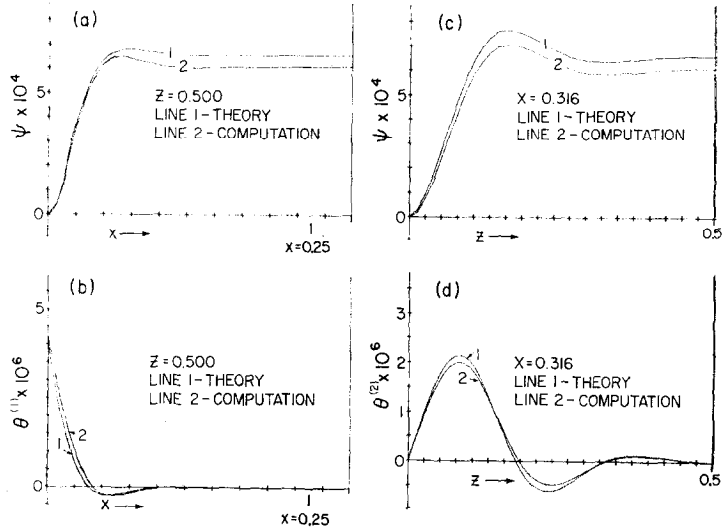

FIG. 13. Comparison between theory, line 1, and computation, line 2 for case 1, $\phi = 0.1°$. Line 1 in (a) is $\psi^{(1)} + \psi_0$ and line 1 in (c) is $\psi^{(2)} + \psi_0$ in Eq. (8). Line 1 in (c) represents $\theta^{(1)}$ and line 1 in (d) represents $\theta^{(2)}$ in Eq. (8). Note that the theoretical stream function, ψ, has been divided by $\sigma^{1/2}$ to compare with the finite difference solutions lines 2.

Figures 14a and b show the corner solutions at $z = 0.105$. Note that the total Ψ and T in the region are $\Psi = \psi_0 + \psi^{(1)} + \psi^{(2)} + \psi^{(*)}$, and $T = T_0 + \theta^{(1)} + \theta^{(2)} + \theta^{(*)}$. The contributions of both $\psi^{(*)}$ and $\theta^{(*)}$ are small as seen in Figs. 14a and b (lines 3). The composite solutions compare with the inite difference result reasonably well.

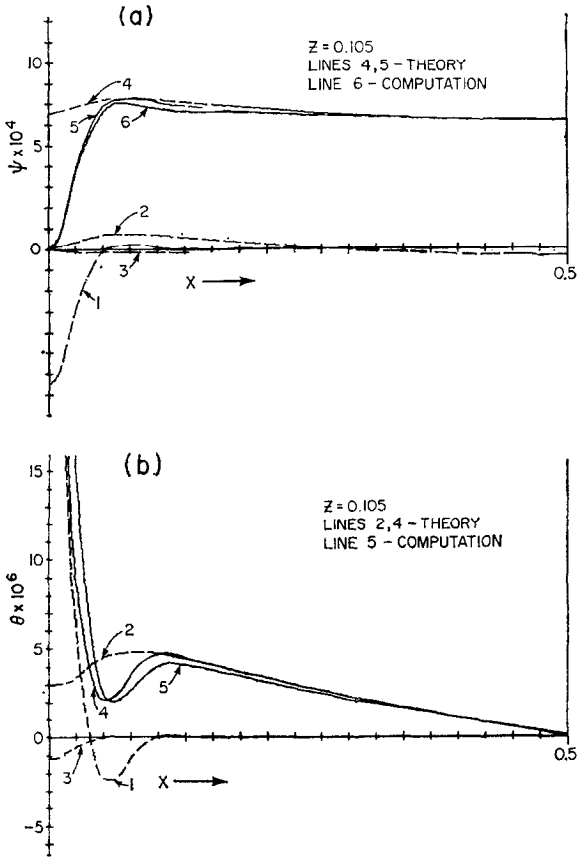

FIG. 14. Comparison of solutions at the corner (0, 0) for case 1. (a) Line 1 is $\psi^{(1)}$, line 2 is $\psi^{(2)}$, line 3 is $\psi^{(*)}$ in Eq. (8g). Near $x = 0$, the solution is line 5 which represents (8i). It asymptotically approaches line 4 which represents $\psi^{(2)} + \psi_0$ as x increases. (b) Line 1 is $\theta^{(1)}$, line 2 is $\theta^{(2)}$, line 3 is $\theta^{(*)}$ in Eq. (8). Equation (8j) is represented by line 4. Note that line 5 in (b) represents $\theta = T - \xi$ from the computation.

ii. *Case* 5, $\phi = \pi/2$

The solutions to be compared are (9). Equations (9c) and (9d) are graphically represented at two values of z in Fig. 15, ($z = 0.105$ and 0.237). Lines 4 represent the finite difference solution and lines 1 represent the composite solutions (9c) and (9d). Lines 3 are the outer layer and lines 2 represent the inner layer. Note that the origin for lines 2 in Figs. 15a and c has been raised for compact presentation. Although the functional forms of lines 1 and 4 agree in general, the magnitude in Fig. 15c is underestimated by at least 20%. The correction temperature θ agrees

very well between the theory and computation at $x = 0$ and asymptotically goes to zero away from the boundary.

One interesting feature the theory produces in Fig. 15b is the S shape of line 1, which is more exaggerated than line 4, the finite difference solution. This S shape is a direct contribution of the inner layer represented by line 2.

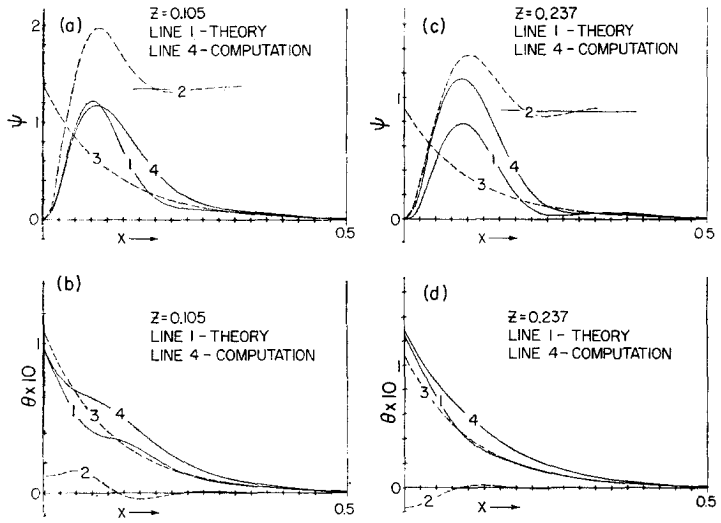

FIG. 15. Comparison of ψ and θ at two levels of z for case 5, $\theta = 90°$. (a, c): Line 2 is the inner layer and line 3 is the outer layer in Eq. (9c) for $z = 0.105$ and $z = 0.237$. Note that the origin of line 2 has been raised for compact presentation by the amount of line 3 at $x = 0$. Line 1 is the composite solution (9c). (b, d): Line 3 is the outer layer and line 2 is the inner layer of θ. Line 1 is the composite solution Eq. (9d). In (a) and (c) the theoretical stream function ψ has been divided by $\sigma^{1/2}$ for comparison.

Figure 16 compares the solutions from Eqs. (9c) to (9f) at two values of x from $z = 0$ to $\frac{1}{2}$. In Figs. 16a and c, lines 3 represent the outer layer contribution which is a linear function of z at given x, or ζ_2, and lines 1 are the composite solutions. Note that although the major contribution to the composite solution is from the outer layer (line 3) as expected, the contributions from the inner layer are not insignificant because they subtract from line 3 as in Fig. 16a, or add to it, as in Fig. 16c, to form the composite solution. Comparing lines 1 and 4 in Figs. 16a and c the two solutions agree pretty well only after the inner solutions have been subtracted and added. Near the boundary at $z = 0$, the proper solution is $\psi^{(3)}$, Eq. (9e), which is graphically represented as lines 2 in Figs. 16a and c. $\psi^{(3)}$ matches onto line 1 asymptotically at $z = 0$. Any connection between lines 1 and 2 can only be constructed heuristically (see [14]).

Similar interpretation also applies to Fig. 16b and d which graphically represent solutions (9d) and (9f). Note that in (9d), the outer layer contribution is a constant at given x (or ζ_2). The contributions from the inner layer (lines 3) are again small but not insignificant to the functional shape of the composite solutions (lines 1). Again lines 1 and 4 are comparable in regions away from $z = 0$. Near the boundary at $z = 0$, $\theta^{(3)}$ in (9f), given as line 2 in Figs. 16b and d, should be compared with lines 4. Lines 2 show that $\theta^{(3)}$ asymptotically match onto $\theta^{(1)}$ at $z = 0$. Again the overall agreement between theory and computation is good.

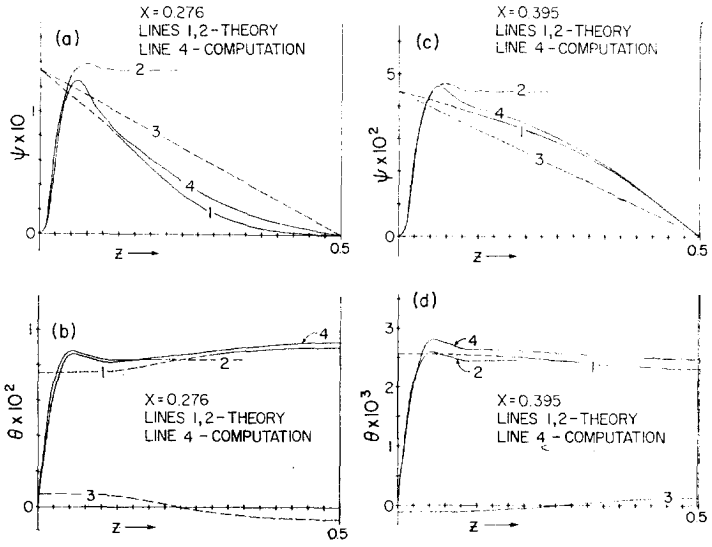

FIG. 16. Comparison of ψ and θ at two levels of x for case 5. (a, c): Line 3 represents the outer layer which is linear in z at given x, and line 1 is the composite solution, Eq. (9c). Near $z = 0$, the solution is Eq. (9e), represented by line 2 which matches asymptotically onto line 1 at $z = 0$. Line 4 is the finite difference solution. (b, d): Line 1 is the composite solution equation (9d) and line 2 represents solution (9f) which matches onto the outer solution. Lines 3 in Fig. 16(b) and (d) represent the inner solution which is z-dependent, and whose magnitude relative to the outer solution diminishes as ζ (or z) increases.

ACKNOWLEDGMENT

The author wishes to thank Dr. S. Blumsack for rewarding discussions and Mr. C. M. Croft for doing the three-dimensional plots. All computations were done on the CDC 3150 in Bedford Institute of Oceanography.

REFERENCES

1. A. ARAKAWA, *J. Computational Phys.* **1** (1966), 119.
2. H. P. GREENSPAN, "The Theory of Rotating Fluids," Cambridge University Press, London/New York, 1968.
3. H. LEVY AND E. A. BAGGOTT, "Numerical Solutions of Differential Equations," Dover, New York, 1950.
4. D. K. LILLY, *Monthly Weather Rev.* **93** (1965), 11.
5. D. K. LILLY, *Geophys. Fluid Dyn.* **3** (1972), 289.
6. O. M. PHILLIPS, *Deep Sea Res.* **17** (1970), 435.
7. C. QUON, Ph. D. Thesis, Cambridge University, 1967.
8. C. QUON, *Phys. Fluids Suppl.* II, **12** (1969), II 214.
9. C. QUON, *Phys. Fluids* **15** (1972), 12.
10. C. QUON, *J. Computational Phys.* **20** (1976), 442.
11. C. QUON, *Tellus*, in press.
12. R. D. RICHTMYER AND K. W. MORTON, "Difference Methods for Initial-Value Problems," Interscience, New York, 1967.
13. K. STEWARTSON, *J. Fluid Mech.* **3** (1957), 17.
14. M. VAN DYKE, "Perturbation Methods in Fluid Mechanics," Academic Press, New York/London, 1964.
15. R. S. VARGA, "Matrix Iterative Analysis," Prentice–Hall, Englewood Cliffs, N.J., 1962.
16. G. VERONIS, *Ann. Rev. Fluid Mech.* **2** (1970), 37.
17. C. WUNSCH, *Deep Sea Res.* **17** (1970), 293.